Dynamic recovery and dynamic recrystallization competition on a Nb- and N-bearing austenitic stainless steel biomaterial: Influence of strain rate and temperature

R.C. Souza [a], E.S. Silva [b], A.M. Jorge Jr. [b,*], J.M. Cabrera [c], O. Balancin [b]

[a] Federal University of Maranhão – UFMA, São Luis, MA, Brazil
[b] Federal University of São Carlos – UFSCar, São Carlos, SP, Brazil
[c] Universitat Politécnica de Catalunya – UPC, Barcelona, Spain

ARTICLE INFO

ABSTRACT

The objective of this study was to investigate the dynamic softening behavior of an austenitic stainless steel with high nitrogen (type ISO 5832-9) through hot torsion tests, in the temperature range of 900–1200 °C and in the strain rate range of 0.01–10 s^{-1}. The shape of flow stress curves indicated that the softening was promoted by dynamic recovery followed by dynamic recrystallization with high level of recovery. The microstructure evolution indicated that even though after large straining as that of the steady state stresses a combination of strained and recrystallized grains was observed. The delay of dynamic recrystallization, which is a consequence of the intermediate level of stacking fault energy of this steel, and the presence of large recrystallized grains, inside of necklace formed by small grains, were associated with extended recovery regions.

1. Introduction

Austenitic stainless steels have outstanding resistance to corrosion and appropriate combination of mechanical properties for many industrial applications. However, when in contact with human-body fluids and tissues in orthopedic implants, they may present several problems such as susceptibility to localized corrosion promoting pitting and crevice corrosion. For instance, the austenitic stainless steel ASTM F 138 is widely used in temporary implants [1] due to its low cost, but its susceptibility to localized corrosion limits its use in permanent orthopedic implants. In the last two decades, the austenitic stainless steel ISO 5832-9 with high nitrogen content has been used as an alternative to ASTM F 138. This steel even in annealed condition has high strength and high resistance to localized corrosion [2,3]. In order to optimize strength and corrosion resistance an appropriate microstructure must be attained. This microstructure, for a given chemical composition, in turn depends on the thermomechanical treatment impaired to the steel during its fabrication.

The operation of different metallurgical phenomena during hot deformation of metallic materials, including work hardening, dynamic recovery and dynamic recrystallization, can lead to changes in the microstructure of the deformed material which are directly reflected in the flow stress curves. At the beginning of straining, there is an increase in the work hardening due to dislocation generation and accumulation. As the deformation continues, part of the stored energy is released with the dislocation annihilation through dynamic recovery. As a consequence, the stress level increases and can find a stationary state in materials with high level of stacking fault energy (SFE) [4]. However, in metals with low SFE, where the rate of dislocation annihilation is usually lower than their rate of generation, there is an increase in the work hardening at the beginning of deformation, until the dislocation density reaches a critical value, that is associated with critical strain (ε_c) necessary to promote the nucleation of new grains [5,6]. It is widely established that before the onset of recrystallization, grain boundaries are extended along the deformation direction, showing serrations and bulges along the grain boundary. If the new grains are small and located along old grain boundaries, it is said that dynamic recrystallization occurs by the necklace mechanism. Increasing deformation, the stress reaches a maximum value, called peak stress (σ_p). The stress level only decreases when the recrystallized volume fraction is large enough to balance the hardening. Further deformation decreases the stress to steady state stress (σ_{ss}). At this moment, the recrystallized microstructure is formed by equiaxed grains. The behavior of dynamic recrystallization is greatly affected by deformation conditions, i.e., temperature and strain rate [7–9].

* Corresponding author. Tel.: +55 16 33518531; fax: +55 16 33615404.
E-mail addresses: moreira@dema.ufscar.br, moreira@ufscar.br (A.M. Jorge Jr.).

Austenitic stainless steels are usually considered as materials having low and intermediate SFE. For instance, the SFE of ASI 304L is about 18 mJ/m^2, while that of AISI 305 is about 34 mJ/m^2, AISI 310S about 94 mJ/m^2, and AISI 316 about 78 mJ/m^2 [10]. The contribution of Ni, Cr, Mn and Mo to the SFE of an austenitic stainless steel matrix was estimated and the calculated SFE for ISO 5832-9 was found to be 68.7 mJ/m^2 [11]. It has been observed that this intermediate level of SFE renders this material prone to cross slip and climb of dislocations, promoting high levels of recovery. High levels of softening of as much as 60% can be promoted by static recovery after hot deformation before and upon the onset of recrystallization [11]. Upon deformation, it has also been observed that, due to high levels of softening promoted by dynamic recovery, a mixture of recrystallized and pancake grains may be present after large straining to steady state stresses [12]. The main purpose of this work was to study the dynamic softening behavior and the microstructural evolution during the progress of dynamic recrystallization, under various conditions of deformation, for ISO 5832-9 biomaterial steel.

2. Experimental procedure

The austenitic stainless steel used in this work, whose chemical composition is given in Table 1, was supplied by Villares Metals, São Paulo, Brazil. The steel had been previously hot rolled to 20 mm diameter bars, annealed at 1030 °C during 60 min and water quenched. Cylindrical specimens with 5 mm effective radius and 10 mm length were machined out of the bars. Mechanical tests were carried out on a computerized TermoMec hot torsion machine model TMIII. In this equipment the instantaneous torque and rotation angle are recorded during testing. Torque is measured by a flange to flange reaction-type torque sensor with resolution, after amplification and digital conversion, of the 0.009 Nm. Rotation angles are measured by an incremental encoder with resolution of about 0.006 rad. The samples were heated in an induction furnace mounted directly on the test machine. The temperature was measured by using an optical pyrometer with final resolution of 0.1 °C. The data were processed using a software program that imposes the parametric tests such as temperature, holding time, amount of straining and strain rate.

Hot torsion tests were carried out over the temperature range of 900–1200 °C and at strain rates in the range of 0.01–10 s^{-1}. The samples were heated from room temperature to 1250 °C with a rate of the 2 °C/s, held for 600 s, cooled down to the deformation temperature with a rate of the 2 °C/s and then held for 30 s before being deformed. In order to correlate the microstructure with the deformation behavior of this steel, two types of test were performed in this investigation. In the first, samples were isothermally strained to $\varepsilon = 4.0$ to determine the flow stress curves; in the second, tests were interrupted at selected strains and the samples were water quenched immediately after deformation to follow the microstructure evolution. In this equipment, water injection is conducted by the software program that controls an electromagnetic valve which is connected with water under pressure; water achieves the sample in a time smaller than 1 s after the straining end.

Equivalent tensile true stress or von Misses true stress (σ), Eq. (1), was obtained from measured torque (M), and equivalent

tensile true strain or von Misses true strain (ε), Eq. (2), was obtained from measured angular displacement (θ, in radians), using the Von Mises criterion and the methodology proposed by Fields and Backofen [13]:

$$\sigma = \frac{\sqrt{3}M}{2\pi r^3}(3 + m + n) \qquad (1)$$

$$\varepsilon = \frac{\sqrt{3}r\theta}{3L} \qquad (2)$$

where r is the radius of the specimen test section, L is the gage length of the specimen, $m = \partial M / \partial \log \theta$ at constant strain, and $n = \partial \log M / \partial \log \theta$ at constant strain rate.

By applying Eqs. (1) and (2) to the specimen size used in this work, the true-stress final resolution is about 0.05 MPa (it will depend on m and n) and the true-strain final resolution is 0.0018.

It is noteworthy that since the 60 years in the last century, studies of deformation under hot work conditions and physical simulation of thermomechanical processing have been widely conducted by torsion testing [14–33]. This has been motivated by some features of this deformation mode. In this work, the experiments were designed to follow the evolution of the work hardening, recovery and recrystallization phenomena; materials with high and intermediate level of SFE trend to be softened by extended recovery and recrystallization can occur just after larger deformations. Upon torsion testing the sample is subjected to shear stresses, as a consequence, the sample transversal area does not change and large straining can be applied. The amount of straining imposed by laboratory methods such as tensile testing and compression testing is not enough to conduct studies at large deformations as necessary for this research.

To correlate the microstructure with the deformation conditions, the samples were water-quenched immediately after deformation. As strain, strain rate and microstructures vary along the radius of the gage section, as usual, metallographic observations were carried out in an axial-diametral cross section of the sample. For this purpose, samples were polished and electrolytically etched in a 65% HNO$_3$ solution. The microstructures were observed by optical and scanning electron microscopy. The recrystallized grain size measurements were performed using an image analysis system and a minimum of 500 grains were measured for each analyzed sample. Differentiation between recrystallized and recovery regions was made by considering microstructural features such as grain size and grain shape, the presence of necklace-kind recrystallization mechanism and twin boundaries, and the appearance of the grain boundaries (serrated or not).

3. Results

3.1. Stress–strain curves

Fig. 1 depicts the plastic flow curves determined for the austenitic stainless steel. In general, the flow stress rose in the initial work-hardening regime, reaching a maximum before dropping in the softening regime. The shape of the flow stress curve changed in both regions as the deformation conditions were changed; this variation was more noticeable in the softening regime. Three different shapes of flow stress curves representing the dissipative nature were observed: (i) stress softening after the peak, leading to a steady state at higher strains, (ii) continuous flow softening until material failure and (iii) flat top flow stress curves.

Also, some difference could be seen in the work-hardening regime; the slopes of the flow stress curves changed, but not as usually. In the initial work-hardening regime ($\theta = d\sigma/d\varepsilon$), the

Table 1
Chemical composition of the austenitic stainless steel biomaterial (wt%).

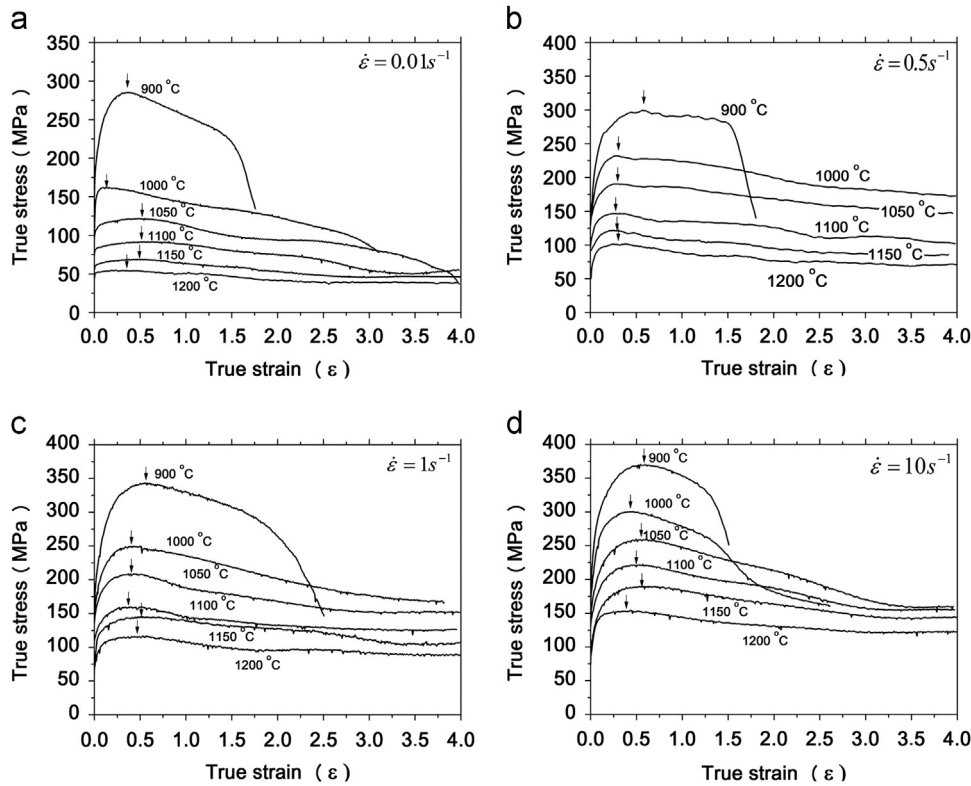| C	Si	Mn	Ni	Cr	Mo	S	P	Cu	N	Nb	Fe
0.035	0.37	4.04	10.6	20.3	2.47	0.0018	0.013	0.06	0.36	0.29	Bal.

Fig. 1. Flow curves for the stainless steel subjected to different strain rates and temperatures: (a) 0.01 s^{-1}, (b) 0.5 s^{-1}, (c) 1 s^{-1} and (d) 10 s^{-1}.

growth of dislocation density (ρ) during deformation (ε) is controlled by the competition between storage and annihilation of dislocations. The contribution of work hardening and the dynamic recovery to the change of dislocation density with deformation (dρ/dε) may be described by the difference between work-hardening term (h) and the dynamic recovery term ($r\rho$). As r and h are independent of the deformation and taken $\sigma = \alpha\mu b(\rho)^{1/2}$, by integration it is attained the dynamic recovery flow stress curve [34]

$$\sigma = [\sigma_{sat}^2 - (\sigma_{sat}^2 - \sigma_0^2)\exp(-r\varepsilon)]^{1/2}$$

where the initial stress for plastic flow (σ_0), saturation stress (σ_{sat}) and strain (ε) are analytically determined from the experimental flow stress curves. The literature has been shown that the value of the recovery parameter (r) (which specifies the "curvature" of the dynamic recovery curve) can be determined from the stress–strain curve. After differentiation and some manipulations of this equation, it is obtained [34]:

$$\sigma\left(\frac{d\sigma}{d\varepsilon}\right) = 0.5r\sigma_{sat}^2 - 0.5r\sigma^2$$

The slop of the $\theta\sigma$ vs. σ^2 curve in the hardening region is given by $m = -0.5r$. Fig. 2 displays the evolution of recovery parameter with the deformation conditions determined for the studied stainless steel. In this figure one can observe that the recovery parameter increases as deformation temperature increases and the applied strain rate decreases. Also, it is worth noticing that the level of $r(6.8$–$26.8)$ is relatively high when compared with values determined for other steels. For instance, values between 2 and 10 were found in microalloyed [35] and in low carbon steels [34] and between 2 and 7 in 304 austenitic stainless steel [36].

The commencement of the work-softening region on the flow stress curves is determined by the critical strain required to trigger the dynamic recrystallization. In order to determine the onset of dynamic recrystallization, diagrams of work-hardening rate
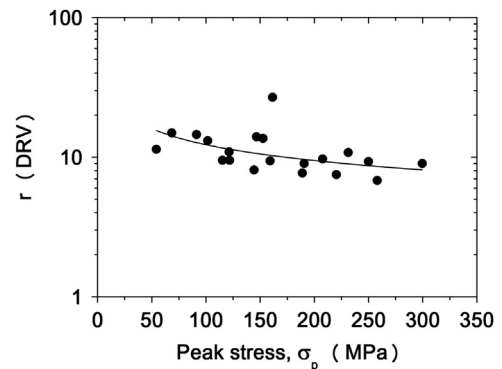

Fig. 2. Dependence of dynamic recovery rate term with deformation conditions.
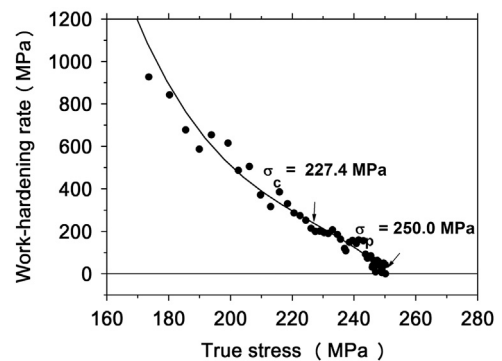

Fig. 3. Dependence of the work-hardening rate (θ) with the applied stress.

($\theta = d\sigma/d\varepsilon$) vs. applied stress were drawn up for the hardening region of the flow stress curves, as displayed in Fig. 3, for the experiment conducted at 1000 °C and 1.0 s^{-1}. This figure shows
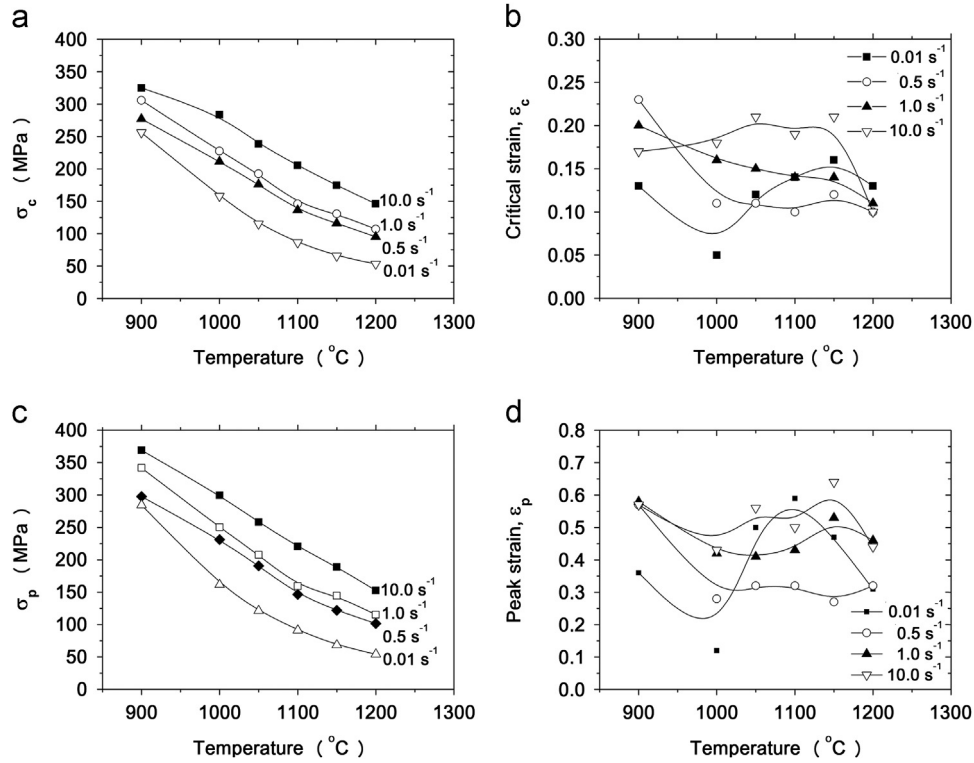
Fig. 4. Dependence of the critical and peak stresses and strains with temperature and strain rate.

that the work-hardening rate continuously decreases as the applied stress increases, displaying an inflection point close to the peak stress ($\theta=0$); this point corresponds to the onset of dynamic recrystallization. The identification of this inflection point is not easy since the noise level of the experimental data causes a large spread during the data processing involved in the calculation of the work-hardening rate. To identify the inflection point it has been suggested a third order polynomial curve fitting to the work-hardening vs. applied stresses [37], as showed in this figure. In this case, the stress associated with the critical strain is close to 227 MPa.

Fig. 4 displays the dependence of critical stress for the onset of dynamic recrystallization (σ_c), the peak stress (σ_p) and their associated strains ε_c and ε_p with temperature and strain rate. It is evident that stress values show the expected tendency, i.e., they increase with the strain rate increasing and the decreasing of the deformation temperature. Although some phases can precipitate during cooling in this steel after reheating at high temperatures, for the instance Z-phase, there is no evidence of dynamic pre-cipitation of these phases in any deformation condition. Fine particles formed during deformation increase the material's strength; it was not observed in Fig. 4 any increase in the peak stress with higher rates than the usual as the temperature decreased. However, the strains ε_c and ε_p show an unexpected behavior, at least when compared with that observed in other steels [38,39], where these deformations increase with strain rate and decreasing temperature. In Fig. 4 is not observed a clear trend between the strains (ε_c and ε_p) and temperature. At lower and higher temperatures the strains decrease as the temperature increases as expected. However, at intermediate temperatures the critical and peak strains are approximately constants; at least for testing conducted with 0.5, 1.0 and 10 s^{-1}. The slight sensitivity of the strain to temperature changes means that the peak stresses at intermediate temperatures were displaced toward smaller deformations, leading to higher work-hardening rates.
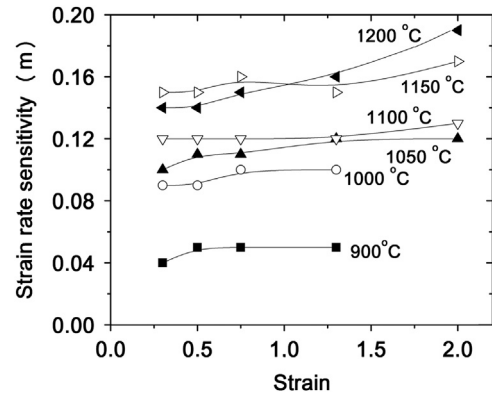

Fig. 5. Dependence of strain rate sensitivity on the amount of strain.

Experimental data clearly show that the flow stress curves features are affected by temperature and strain rate. To analyze the plastic behavior the strain rate sensitivity of the flow stress, m, was determined by using the following equation: $m=\Delta\ln\sigma/\Delta\ln\dot{\varepsilon}$, with temperature and strain constants for a given history. Fig. 5 displays the calculated values of m as a function of the amount of strain and the deformation temperature of the steel under study. This figure indicates that the strain rate sensitivity of flow stress (m) increases with the deformation temperature at the same strain and with the amount of straining at the same temperature. As it is expected m is quite low at lower temperature (0.04) but increases with tem-perature and attains values of the order of 0.17 at higher tem-peratures. The variation in m lies within the range reported in the literature for stainless steels: 0.05–0.23 [40]. The calculated values at 900 °C are two or three-fold lower than those determined at intermediate and high temperatures. This increased strain rate sensitivity at higher temperatures can be associated with the dependence of the SFE level with temperature [40]. At elevated
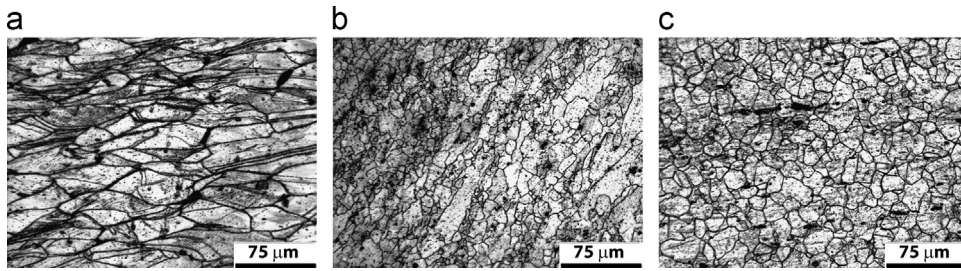
Fig. 6. Microstructures observed after deformation. (a) Strained and recovered grains (900 °C/0.01 s^{-1} and $\varepsilon=1.5$), (b) partially recrystallized structure (1050 °C/10 s^{-1} and $\varepsilon=4.0$), and (c) recrystallized grains (1100 °C/0.01 s^{-1} and $\varepsilon=4.0$).
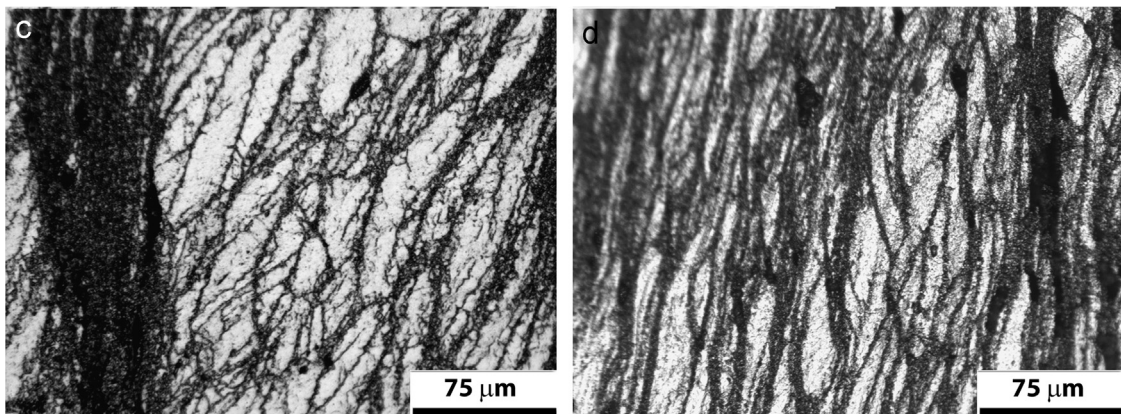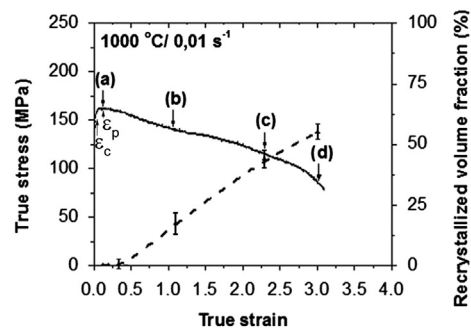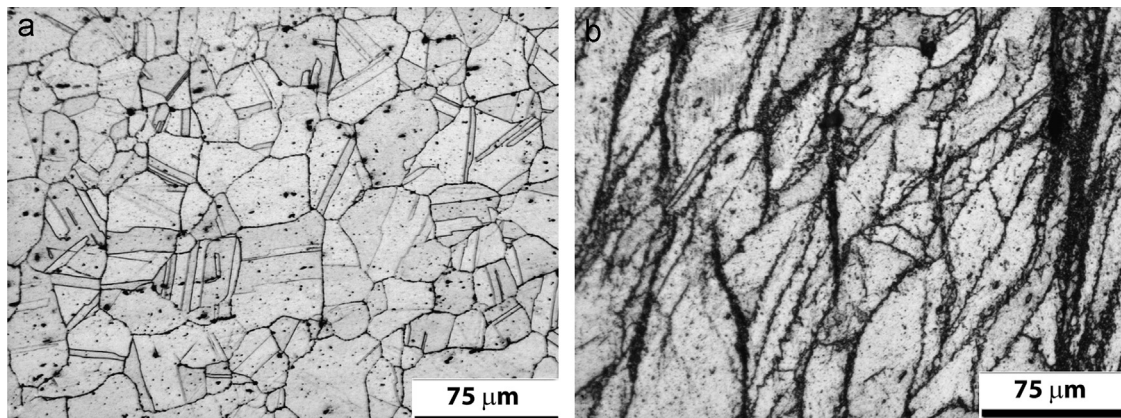

Fig. 7. Flow stress curve and microstructure evolution during straining at 1000 °C and strain rate of 0.01 s^{-1}. The microstructures correspond to the following strains: (a) $\varepsilon=\varepsilon_p=0.11$, (b) $\varepsilon=1.1$, (c) $\varepsilon=2.3$ and (d) $\varepsilon=3.0$.

temperatures the value of SFE increases, which reduces the spacing between the partial dislocations, making the process of recombination easier [40]. This means that at high temperatures the dislocations can recombine, but this level of recombination will reduce at low temperatures since the lower SFE means that the partials are spaced further apart.

3.2. Microstructure evolution

Fig. 6 displays some observed microstructures after deformation in different conditions. Fig. 6a displays strained grains after deformation to 1.5 at 900 °C and strain rate of 0.01 s^{-1}; in this case, deformation was interrupted after the peak stresses (Fig. 1a).
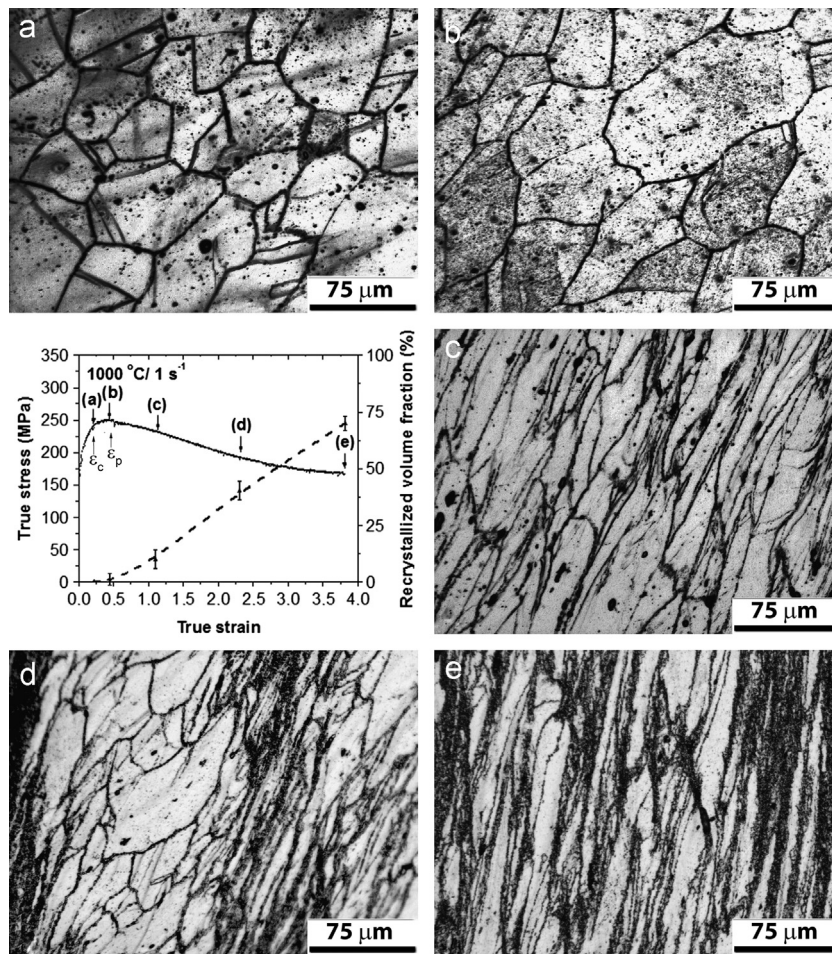
Fig. 8. Flow stress curve and microstructure evolution during straining at 1000 °C and strain rate of 1.0 s⁻¹. The microstructures correspond to the following strains: (a) $\varepsilon=0.22$, (b) $\varepsilon=\varepsilon_p=0.45$, (c) $\varepsilon=1.1$, (d) $\varepsilon=2.3$ and (e) $\varepsilon=4.0$.

The combination of strained and recrystallized grains observed in Fig. 6b was attained after straining to 4.0. In this case, the deformation corresponds to steady state of stresses (Fig. 1d). Fig. 6c displays recrystallized grains obtained after straining to 4.0, steady state of stresses (Fig. 1a). At first glance, one can say that the observed microstructures do not represent that which are expected to be attained after straining to those interruption points on the flow stress curves. To investigate the microstructure evolution during hot deformation six different deformation conditions were analyzed: 1000 °C with strain rates of 0.01 s⁻¹ and 1 s⁻¹, 1100 °C with strain rates of 0.01 s⁻¹, 0.5 s⁻¹ and 1.0 s⁻¹ and 1200 °C with strain rate of 0.5 s⁻¹. Together with the observed microstructures, Figs. 7–12 display the points in the flow stress curves where straining were interrupted and the suitable recrystallized volume fractions.

Fig. 7 displays the observed microstructure evolution after deformation at 1000 °C with strain rate of 0.01 s⁻¹. At peak stress ($\varepsilon=0.12$), the microstructure was lightly strained, as observed in Fig. 7a, indicating that the dynamic recrystallization had not started yet, although the straining was larger than the critical strain. New grains were observed to nucleate at old grain boundaries after straining to $\varepsilon=1.1$ (Fig. 7b), and followed forming as deformation proceeded (Fig. 7c and d); the recrystallized volume fraction increased as the straining enlarged. However, even though after large deformation the dynamic recrystallization had not completed yet; the recrystallized volume fraction on the fractured sample ($\varepsilon=3.0$) was close to 0.55. Also, it is noteworthy that the

flow stress level decreases continuously after the peak stress without reaching a steady state stress. Hence, the concentration of new grains around old grain boundaries and the shape of flow stress curve suggest that strain localization took place.

The microstructure evolution during deformation at 1000 °C with strain rate of 1.0 s⁻¹ is displayed in Fig. 8. The microstructure after straining to critical strain and peak stress displayed deformed grains with some serrated grain boundary (Fig. 8a and b), but new recrystallized grains were observed only after large deformation as $\varepsilon=1.1$ (Fig. 8c). After this straining, the nucleation along grain boundaries proceeded (Fig. 8d). However, the recrystallization had not completed even though with straining to $\varepsilon=4.0$ (Fig. 8e), where the recrystallized volume fraction was closed to 0.7. In this experiment the material's behavior is very similar to that observed with strain rate of 0.01 s⁻¹: localized flow took place as indicated by continuous flow softening and concentration of new grains around old grain boundaries.

Fig. 9 displays the microstructure evolution observed after deformation at 1100 °C and strain rate of 0.01 s⁻¹. Microstructure of strained sample to critical strain (Fig. 9a) showed deformed grains with serrated grain boundaries. Small grains at old grain boundaries were observed after straining to peak strain (Fig. 9b), indicating that new grains had formed by necklace mechanism. With the continuity of straining, the nucleation process continued to increases the recrystallized volume fraction, but without the recrystallization is completed, as can be seen in Fig. 9e, where the recrystallized volume fraction is close to 0.75. The recrystallized
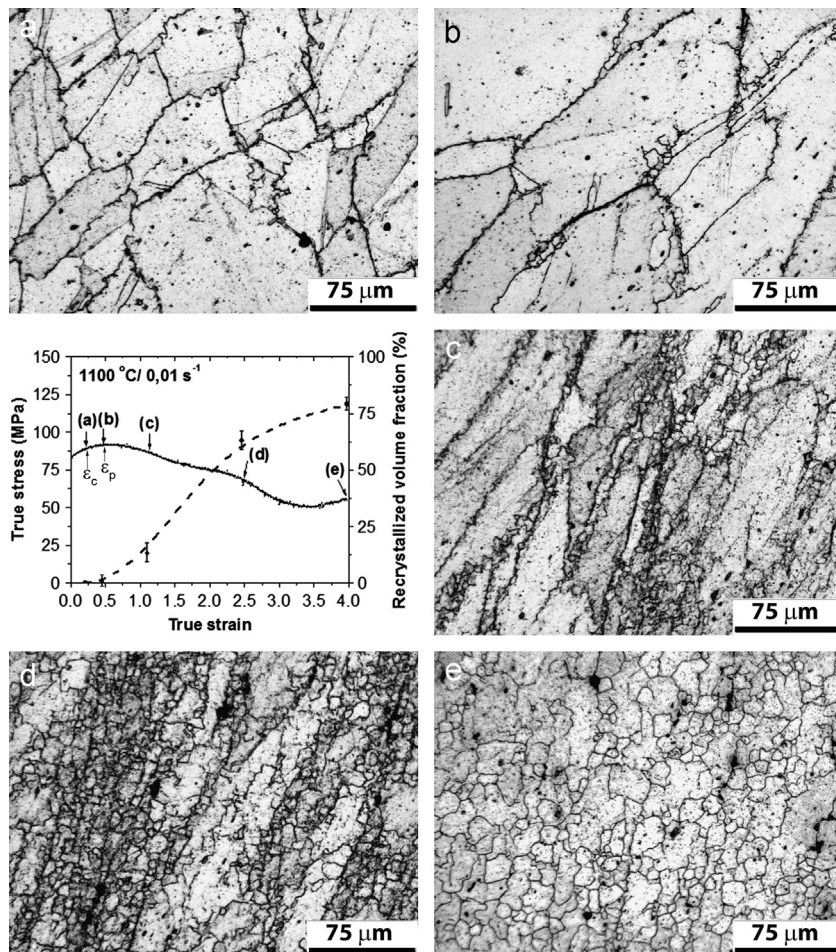
Fig. 9. Flow stress curve and microstructure evolution during straining at 1100 °C and strain rate of 0.01 s^{-1}. The microstructures correspond to the following strains: (a) $\varepsilon=0.22$, (b) $\varepsilon=\varepsilon_p=0.45$, (c) $\varepsilon=1.1$, (d) $\varepsilon=2.5$ and (e) $\varepsilon=4.0$.

volume fraction curve indicated that a large increase occurred at straining close to 2.5; visible decrease is also observed in the flow stress level. It is worth observing that the new grains formed inside the old grains, after large deformation, are larger than that formed by necklace.

The microstructure evolution during deformation at 1100 °C with strain rate of 0.5 s^{-1} is displayed in Fig. 10. After small deformations (Fig. 10a and b) the grains were lightly strained and the grain boundaries were serrated, indicating that the dynamic recrystallization had not started yet. This trend continued as deformation is increased and a small volume fraction of new grains is showed in Fig. 10c even though the material was subjected to a straining greater than the peak strain. It can be observed that between (c) and (d) the flow stress curve level off, showing a flat flow stress region. As the straining preceded a visible decrease in the stress level was observed and the recrystallized volume fraction increased. After larger straining the dynamic recrystallization rate increased (Fig. 10d and e), but some deformed grains are observed after straining to $\varepsilon=4.0$, where the recrystallized volume fraction is close to 0.95.

Fig. 11 displays the microstructure evolution observed after deformation at 1100 °C and strain rate of 1.0 s^{-1}. After small deformations (Fig. 11a and b) the grains were lightly strained and the grain boundaries were serrated, indicating that the dynamic recrystallization had not started yet. This trend continues as deformation is increased. The microstructure showed in Fig. 11c displays a small volume fraction of new grains even though the

material was subjected to $\varepsilon=1.1$. After larger straining the dynamic recrystallization rate increases (Fig. 11d and e), but some deformed grains are observed after straining to $\varepsilon=4.0$, where the recrystallized volume fraction is close to 0.75.

The microstructure evolution during deformation at 1200 °C with strain rate of 0.5 s^{-1} is displayed in Fig. 12. After deformation to critical strain, it is possible to observe some serrated grain boundaries (Fig. 12a). A small volume fraction of new grains was observed after straining to peak stress (Fig. 12b) and flow stress softening after the peak is observed indicating that the dynamic recrystallization had started. As deformation proceeded, the nucleation of new grains continued. After large deformation the recrystallization completed (Fig. 12e), leading to a steady state of stress. The shape of flow stress curve and the evolution of the recrystallized volume fraction are typical of materials that recrystallize dynamically. However, the average grain size is larger, particularly inside the old grains. This suggests that the kinetics of dynamic recrystallization had changed. The formation of new grains inside old grains is more sluggish than that formed by necklace.

The evolution of recrystallized grain size during deformation was measured upon several transient stages of recrystallization. It is worth distinguishing here this transient recrystallized grain size (D_{TRAN}) from that measured after completing recrystallization. Subsequent rounds of recrystallization of the recrystallized material may occur prior to completion of the first wave of recrystallization and the associated kinetics will depend on transient
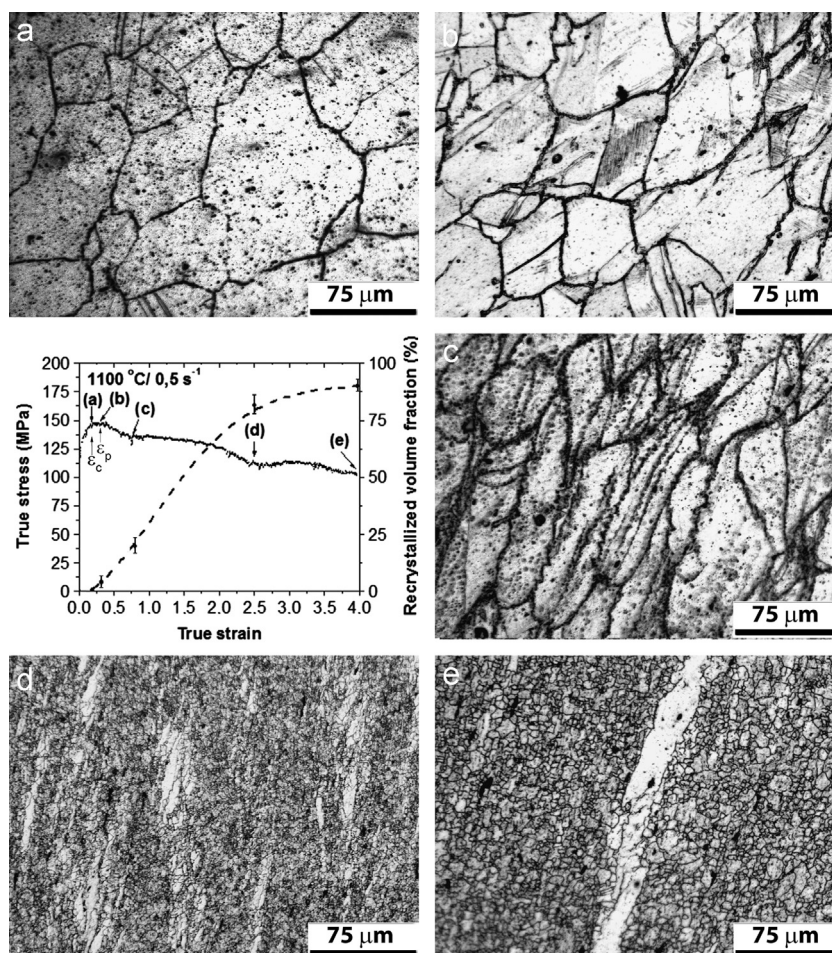
Fig. 10. Flow stress curve and microstructure evolution during straining at 1100 °C and strain rate of 0.5 s^{-1}. The microstructures correspond to the following strains: (a) ε=0.19, (b) ε=0.32, (c) ε=0.80, (d) ε=2.5 and (e) ε=4.0.

recrystallized grain size [41]. Fig. 13 displays the evolution of transient recrystallized grain size with the amount of strain and deformation temperature. At lower temperatures, when the recrystallization was not completed, the transient grain size is maintained at relatively fine level since the prevailing nucleation mechanism was necklace. However, at elevated temperatures, the transient recrystallized grain size increases as recrystallization progresses. As a consequence larger grains surrounded by small grains formed by necklace mechanism were observed.

In order to confirm the combination of recrystallized and recovery regions observed by optical microscopy, samples with different recrystallized volume fraction were observed by Electron Backscattered Diffraction (EBSD) through scanning electron microscopy. Fig. 14 displays images from two observations: dynamic recovered microstructure with small recrystallized volume fraction nucleated at old grain boundaries by necklace mechanism and large recrystallized volume fraction displaying new grains with great heterogeneity in grain size.

4. Discussion

Stacking fault energy (SFE) influences dislocation climb and cross slip, which are dominant factors in metal working. The SFE of austenitic (fcc) phase of the Fe–Cr–Ni alloys depends on the exact composition of the steel and generally ranges from 10 to 100 mJ/m^2 (1 mJ/m^2=1 erg/cm^2). The SFE calculated for ISO 5832-9 was

found to be 68.7 mJ/m^2 [11]. When this value is compared with that found for other materials, for instance: the SFE of pure silver is about 22 mJ/m^2, pure Cu about 78 mJ/m^2 and aluminum is 200 mJ/m^2: the ISO 5832-9 steel can be considered as a material with an intermediate level of SFE.

During high temperature deformation, unstable microstructure work hardens and softens by dynamic recovery and dynamic recrystallization. The extent of recovery is governed by deformation conditions and material characteristics such as SFE. It is well known that dislocation mobility depends on the SFE, which, by affecting the extent to which dislocation dissociates, determines the rate of dislocation climb and cross slip. In metals and alloys with high SFE, climb is rapid and significant recovery may occur, while metals with relatively low SFE, in which cross slip and climb dislocation are difficult, show little recovery of dislocation structure prior to recrystallization.

The extent of the softening promoted by dynamic recovery before the onset of dynamic recrystallization affects the shape of flow stress curves. When straining is performed at a constant temperature and strain rate, the flow stress rises in the initial work-hardening regime and then becomes constant in materials with high SFE; by contrast, it experiences a maximum before dropping to the steady state in low SFE steels. It is possible to see some combination of these (kinds) shapes of flow stress curves in Fig. 1. At lower temperatures and intermediate strain rates (for instance with strain rate of 0.5 s^{-1} and temperature range from 900 to 1100 °C), the flow stress curves present regions of flat type,
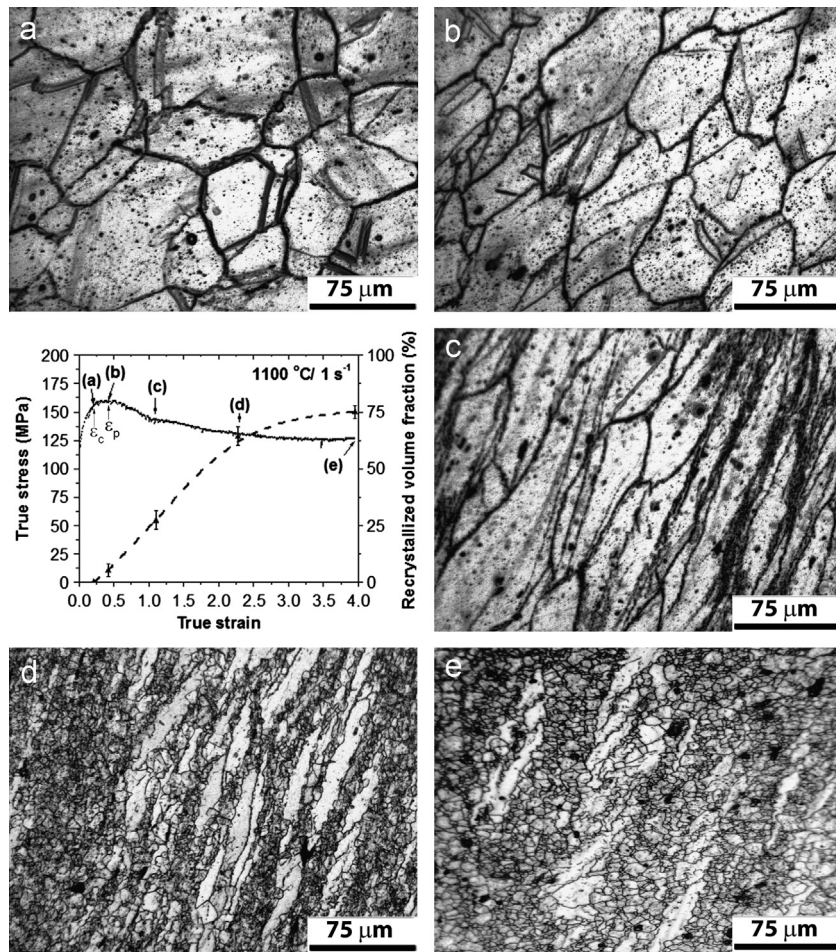
Fig. 11. Flow stress curve and microstructure evolution during straining at 1100 °C and $\dot{\varepsilon}=1$ s^{-1}. The microstructures correspond to the following strains: (a) $\varepsilon=0.21$, (b) $\varepsilon=0.42$, (c) $\varepsilon=1.1$, (d) $\varepsilon=2.3$ and (e) $\varepsilon=4.0$.

where the stress does not vary with strain, as observed in materials that dynamically recover through the softening process. At higher temperatures and lower strain rates, flow softening after a peak stress, leading to a steady state at higher strains, as observed in materials that softening by dynamic recrystallization, as can be seen at 1200 °C.

Microstructures displayed in Section 3.2 clearly show that the softening observed during straining was promoted by recovery and recrystallization. At the beginning of every deformation, the microstructure consists of grains lightly deformed with some serrated grain boundaries. These are typical features of dynamic recovery. As the deformation proceeds new grains are observed in older grain boundaries, indicating that recrystallization had already started. And after larger straining, the samples were partially or totally recrystallized. To confirm the features observed by optical microscopy, EBSD was conducted as displayed in Fig. 14. Grains formed by necklace at old grain boundaries and dislocation substructures inside the old grains are observed in Fig. 14a. New grains with different sizes together with regions that were still not recrystallized are observed in Fig. 14b.

All the observed microstructure evolution indicated that the softening took place by the combination of recovery and recrystallization and the fraction of each one depends on deformation conditions, as can be seen in Figs. 7–12. At lower temperatures, recovery is the major mechanism (Figs. 7 and 8), while at higher temperatures full recrystallized microstructure can be observed (Fig. 12). However, it is worth noticing that dynamic

recrystallization was retarded in every experiment conducted here. New grains were observed only after the peak stresses, which is away from the critical strain for the onset of dynamic recrystallization. Also, it was observed strained old grains in the steady state of stresses, where only recrystallized grains were expected. Although the critical strain for onset of dynamic recrystallization determined here, following the procedure indicated in the literature, was not confirmed by microstructure observation, it must be taken into account that, when a third order polynomial equation is fitted on to work hardening vs. applied stress diagram, an inflexion point will be found independently of it actually exist or not.

To investigate the dynamic recrystallization delay, the work hardening region of the flow stress curves should be analyzed. Fig. 4 showed that the peak strain, which outline the work-hardening region, does not present the usual behavior observed in material that soften by dynamic recrystallization: it is little sensitive to the deformation temperature. In this region work hardening, dynamic recovery and dynamic recrystallization can act simultaneously. The action of dynamic recovery reduces the work-hardening rate and the flow stress plateaus to a constant value identified as saturation stress. Since the interpartial dislocation spacing in high (and intermediate) SFE materials is quite small, thermal activation provided by high temperatures is sufficient to promote dynamic recovery. However, as the temperature is decreased the recombination of partial dislocations becomes more difficult leading to an increase in the rate of work hardening.
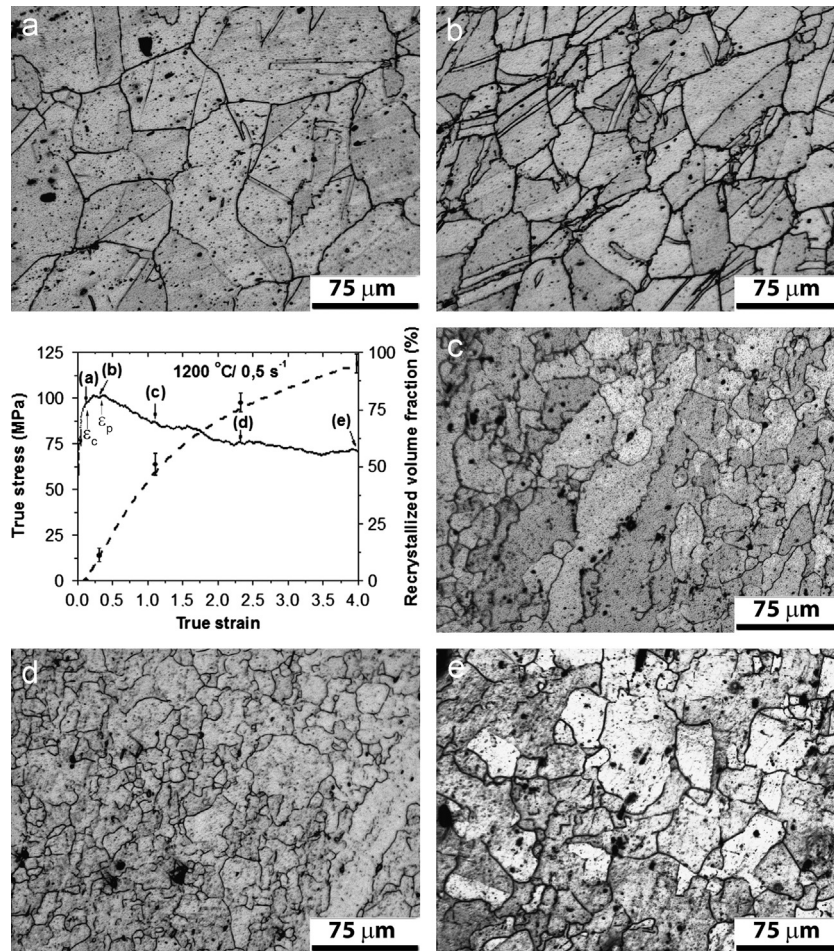
Fig. 12. Flow stress curve and microstructure evolution during straining at 1200 °C and $\dot{\varepsilon}=0.5$ s^{-1}. The microstructures correspond to the following strains: (a) $\varepsilon=\varepsilon_c=0.13$, (b) $\varepsilon=\varepsilon_p=0.31$, (c) $\varepsilon=1.1$, (d) $\varepsilon=2.3$ and (e) $\varepsilon=4.0$.
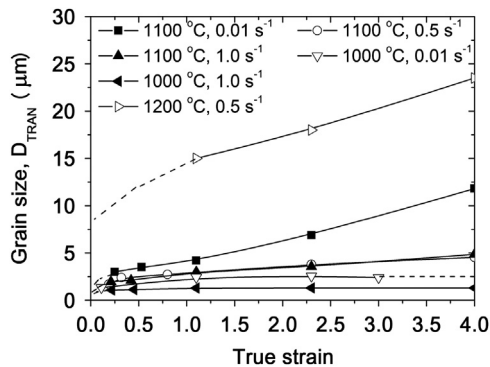

Fig. 13. Dependence of transient recrystallized grain size (D_{TRAN}) on straining during dynamic recrystallization.

As can be seen in Fig. 2 the level of recovery parameter for the steel in study is higher than that observed in other steels. By comparing the dynamic recovery parameter of this steel with that of the AISI 304 type one can infer that the softening promoted by dynamic recovery is more effective in the steel in study. Again, comparing the strain rate sensitivity to flow stress of the ISO 5832-9 (Fig. 5) with data present in the literature for AISI 304 [40], one can infer that at low levels of m (~0.05) the dynamic recovery is sluggish and, as a consequence, the dynamic recrystallization is delayed/inhibited. This postponement takes place on each one

steels at different temperature ranges: 304-type close to 700–800 while in the steel in study at higher temperatures (900–1100 °C).

As a consequence of the dynamic recrystallization delays, the restoration promoted by dynamic recovery proceeds upon deformation and the stored energy is minimized. As observed in Figs. 9–13 the new grains formed within old grains are larger than that formed by necklace mechanism, suggesting a lower nucleation rate. Fig. 15a displays a partially recrystallized microstructure. It is possible to see larger grains inside of the old grains and small grains at old grain boundaries. It is worth noticing that larger grains are formed by the growth of small grains located at grain boundaries. One can infer that, after the formation of the some layers of the necklace, the recrystallization inside of the intensively recovered region proceeds, but with a lower rate than that observed during the necklace formation. As a consequence, grain sizes heterogeneity is observed (Fig. 15b).

5. Conclusions

The shape of flow stress curves changed with deformation conditions and some differences were observed in the parameters that described the material's plastic behavior. The level of the recovery parameter for this steel is higher than those found for other steels, suggesting that softening promoted by dynamic recovery is effective in this steel. Also, the peak strain is little sensitive to deformation temperature.
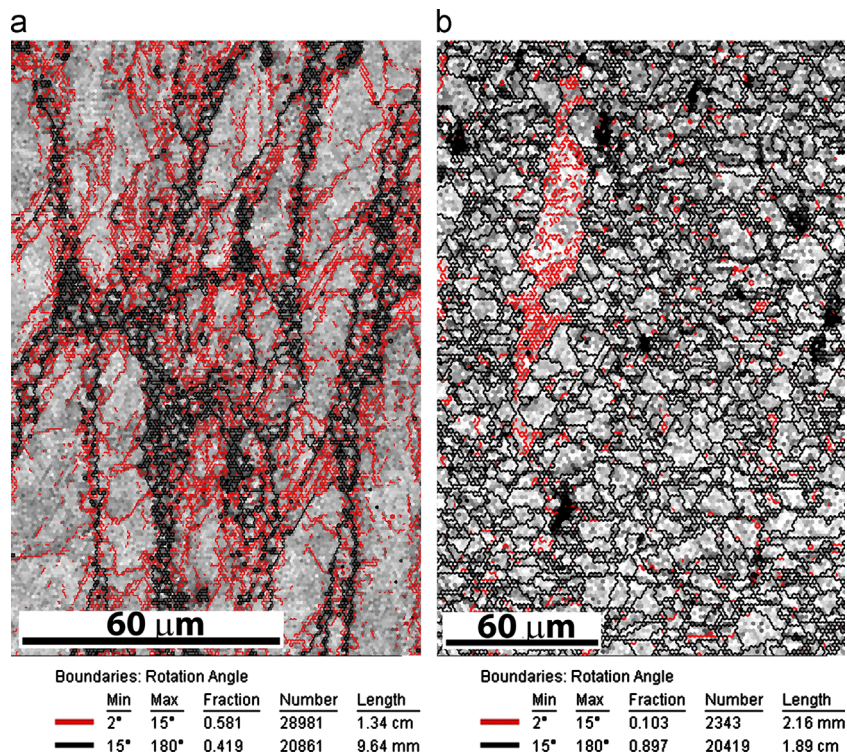
Boundaries: Rotation Angle				
	Min	Max	Fraction	Number	Length
—	2°	15°	0.581	28981	1.34 cm
—	15°	180°	0.419	20861	9.64 mm

Boundaries: Rotation Angle				
	Min	Max	Fraction	Number	Length
—	2°	15°	0.103	2343	2.16 mm
—	15°	180°	0.897	20419	1.89 cm

Fig. 14. EBSD maps showing the microstructure at different stages of deformation. (a) New grains, recovered and strained regions after straining to $\varepsilon = 1.5$ at 1000 °C and 1.0 s^{-1} and (b) recrystallized and recovered regions after straining to $\varepsilon = 2.3$ at 1100 °C and 0.01 s^{-1}.
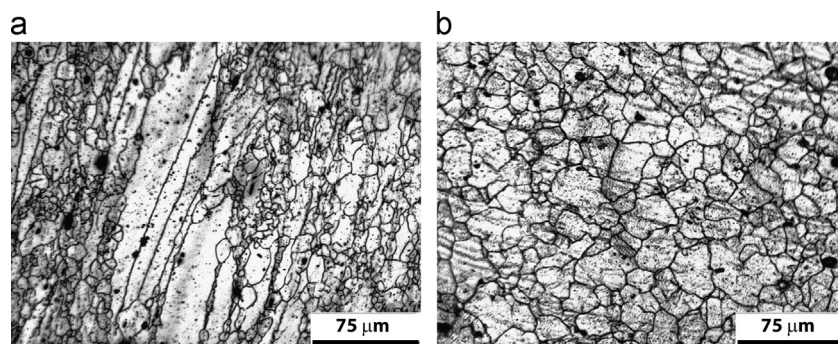

Fig. 15. Microstructures showing recrystallization grain growth observed after straining to $\varepsilon = 4.0$ with strain rate of 10 s^{-1} at (a) 1100 °C and (b) at 1200 °C.

The microstructure evolution indicated that the softening observed during deformation was promoted by recovery and recrystallization. At lower temperatures, recovery is the major mechanism. At intermediate and higher temperatures the samples are partially or totally recrystallized after large straining, showing extended recovery region inside of the old grains or larger recrystallized grains together with small grains formed by necklace mechanism.

The efficiency of recovery upon deformation is associated with the intermediate level of stacking fault energy. As a consequence of the dynamic recrystallization delay, the stored energy is minimized upon deformation, leading to strained and/or large recrystallized grains on the steady state stresses.

References

[1] I. Gotman, J. Endourol. 11 (6) (1997) 383–389.
[2] C. Örnhagen, J.O. Nilsson, H. Vannevik, J. Biomed. Mater. Res. 31 (1996) 97–103.
[3] E.J. Giordani, V.A. Guimaraes, T.B. Pinto, I. Ferreira, Int. J. Fat. 26 (2004) 1129–1136.
[4] A.M. Jorge Jr., W. Regone, O. Balancin, J. Mater. Process. Technol. 142 (2) (2003) 321–415.
[5] E.I. Poliak, J. Jonas, J. Acta Mater. 44 (1996) 127–136.
[6] R.D. Doherty, D.A. Hughes, F.J. Humphreys, J.J. Jonas, D. Juul Jensen, M.E. Kassner, W.E. King, T.R. McNelley, H.J. McQueen, A.D. Rollett, Mater. Sci. Eng. A 238 (1997) 219–274.
[7] M. Jafari, A. Najafizadeh, Mater. Sci. Eng. A 501 (2009) 16–25.
[8] M. El Wahabi, J.M. Cabrera, J.M. Prado, Mater. Sci. Eng. A 343 (2003) 116–125.
[9] T. Sakai, J. Mater. Process. Technol. 53 (1995) 349–361.
[10] R.E. Schramn, R.P. Reed, Metall. Trans. A6 (1975) 1345–1351.
[11] E.J. Giordani, A.M. Jorge Jr., O. Balancin, Scr. Mater. 55 (2006) 743–746.
[12] E.S. Silva, R.C. Sousa, A.M. Jorge Jr., O. Balancin, Mater. Sci. Eng. A 543 (2012) 69–75.
[13] D.S. Fields, W.A. Backofen, Proc. Am. Soc. Test. Mater. (ASTM) 57 (1957) 1259–1272.
[14] C. Rossard, P. Blain, Recherches sur la deformation des aciers a chaud. Publications de 1´Institut de Recherches de la Sidérurgie (IRSID), Série A, no. 174, October 1957.
[15] ISI Publication 108 – Deformation under Hot Working Conditions. The Iron and Steel Institute. Printed by Perivan/WLP Group/Southend-on-sea, 1968, 183 pp.
[16] G. Canova, G.G. Sell, S. Shrivastava, J.J. Jonas, J. Met. 31 (1979) 73–73.
[17] S.L Semiatin, G. Lahoti, J.J. Jonas, Application of the torsion test to determine workability, 9th ed.,ASM Metals Handbook, vol. 8, Metals Park, OH154–184.
[18] N.D. Ryan, H.J. McQueen, J. Mater. Process. Technol. 36 (1993) 103–123.
[19] C. Roucoules, P.D. Hodgson, Mater. Sci. Technol. 11 (1995) 548–556.

[20] C.A. Hernandez, S.F. Medina, J. Ruiz, Modelling austenite flow curves in low alloy and microalloyed steels, Acta Mater. 44 (1996) 155–163.
[21] A. Fernandez, B. Lopez, J.M. Rodriguez-Ibabe, Relationship between the austenite recrystallized fraction and the softening measured from the interrupted torsion test technique, Scr. Mater. 40 (1999) 543–549.
[22] O. Balancin, W.A.M. Hoffmann, J.J. Jonas, Metall. Mater. Trans. A 31A (2000) 1353–1364.
[23] M. Militzer, E.B. Hawbolt, T.R. Meadowcroft, Metall. Mater. Trans. A 31A (2000) 1246–1259.
[24] R. Abad, A.I. Fernandez, B. Lopez, J.M. Rodriguez-Ibabe, ISIJ Int. 41 (2001) 1373–1382.
[25] M.R. Barnett, F. Montheillet, Acta Mater. 50 (2002) 2285–2296.
[26] P.J. Hurley, B.C. Muddle, P.D. Hodgson, Metall. Mater. Trans. A 33A (2002) 2985–2993.
[27] G. Avramovic-Cingara, H.J. McQueen, D.D. Perovic, Mater. Sci. Technol. 19 (2003) 11–19.
[28] P.D. Hodgson, S.H. Zahiri, J.J. Whale, ISIJ Int. 44 (2004) 1224–1229.
[29] G. Azevedo, R. Barbosa, E.V. Pereloma, D.B. Santos, Mater. Sci. Eng. A 402 (2005) 98–108.
[30] H. Beladi, G.L. Kelly, P.D. Hodgson, Metall. Mater. Trans. A 38A (2007) 450–463.
[31] A. Abdollah-Zadeh, B. Eghbali, Mater. Sci. Eng. A 457 (2007) 219–225.
[32] S. Spigarelli, M. El Mehtedi, P. Ricci, C. Mapelli, Mater. Sci. Eng. A 527 (2010) 4218–4228.
[33] A.M. Jorge Jr., L.H. Guedes, O. Balancin, J. Mater. Res. Technol. 1 (2012) 141–147.
[34] J.J. Jonas, X. Quelennec, L. Jiang, E. Martin, Acta Mater. 57 (2009) 2748–2756.
[35] A. Laasraoui, J.J. Jonas, Metall. Mater. Trans. A 22A (1991) 1545–1558.
[36] A.M. Jorge Jr., O. Balancin, Mater. Res. 8 (2005) 309–315.
[37] A. Najafizadeh, J.J. Jonas, ISIJ Int. 46 (2006) 1679–1684.
[38] I. Mejía, A. Bedolla-Jacuinde, C. Maldonado, J.M. Cabrera, Mater. Sci. Eng. A 528 (2011) 4133–4140.
[39] E.I. Poliak, J.J. Jonas, ISIJ Int. 43 (2003) 684–691.
[40] A.S. Taylor, P.D. Hodgson, Mater. Sci. Eng. A 528 (2011) 3310–3320.
[41] M.C. Mataya, E.R. Nilsson, E.L. Brown, G. Krauss, Metall. Mater. Trans. A 34A (2003) 1683–1703.